



# Titanium Based Materials for High-Temperature Gas Sensor in Harsh Environment Application<sup>†</sup>

Roussin Lontio Fomekong<sup>1,\*</sup>  and Bilge Saruhan<sup>2</sup> 

<sup>1</sup> Higher Teacher Training College, University of Yaounde I, Yaounde P.O. Box 47, Cameroon

<sup>2</sup> Department of High-Temperature and Functional Coatings, Institute of Materials Research, German Aerospace Center (DLR), 51147 Cologne, Germany; bilge.saruhan@dlr.de

\* Correspondence: lonforou@yahoo.fr or roussin.lontio@univ-yaounde1.cm

<sup>†</sup> Presented at the 1st International Electronic Conference on Chemical Sensors and Analytical Chemistry, 1–15 July 2021; Available online: <https://csac2021.sciforum.net/>.

**Abstract:** Gas selective sensors that are capable of sensing at hot-gas environment are increasingly gaining importance for the monitoring of combustion and thermal processes releasing NO, NO<sub>2</sub> and H<sub>2</sub> containing hot gases at temperatures exceeding 600 °C. Despite some drawbacks, TiO<sub>2</sub> is capable of operating as a gas sensor above 500 °C. In this context, Ni-doped TiO<sub>2</sub>, Co-doped TiO<sub>2</sub> and Rh-doped BaTiO<sub>3</sub> have been prepared by oxalate coprecipitation route and fully characterized. Co-doping of TiO<sub>2</sub> promotes p-type behavior exhibiting good sensing properties to NO<sub>2</sub> while Ni-doping displays the maintenance of n-type behavior and better H<sub>2</sub>-sensing properties at 600 °C. Rh-doped BaTiO<sub>3</sub> shows excellent NO sensing properties at 900 °C.

**Keywords:** Ni-doped TiO<sub>2</sub>; Co-doped TiO<sub>2</sub>; Rh-doped TiO<sub>2</sub>; coprecipitation; high-temperature gas sensor



**Citation:** Fomekong, R.L.; Saruhan, B. Titanium Based Materials for High-Temperature Gas Sensor in Harsh Environment Application. *Chem. Proc.* **2021**, *5*, 66. <https://doi.org/10.3390/CSAC2021-10480>

Academic Editor: Huangxian Ju

Published: 30 June 2021

**Publisher's Note:** MDPI stays neutral with regard to jurisdictional claims in published maps and institutional affiliations.



**Copyright:** © 2021 by the authors. Licensee MDPI, Basel, Switzerland. This article is an open access article distributed under the terms and conditions of the Creative Commons Attribution (CC BY) license (<https://creativecommons.org/licenses/by/4.0/>).

## 1. Introduction

High temperature gas sensors are mainly designed to solve gas detection and monitoring problems with a high operating temperature environment, such as gas turbine, nuclear power plants and automobile internal combustion engine emission [1]. As far as target gases are concerned NO<sub>x</sub> (NO<sub>2</sub>, NO) and H<sub>2</sub> are among the most important. NO<sub>x</sub> is a severely toxic gas with a pungent odor arising mostly from the related human activities involving high temperature such as combustion of coal and oil at electric power plants, combustion of chemical plant and also in emissions from automotive and aircraft engines. NO<sub>x</sub>-emission leads to harmful effects on the environment and health. There is an urgent need to develop sensor control systems for exhaust emission gases to directly monitor NO<sub>x</sub> at temperatures in the range of 400–900 °C [2]. As far as hydrogen is concerned, it is the best candidate to replace the hydrocarbon-based fuels used in many combustion engines such as those in automobiles and aircraft, which are responsible for much of today's air pollution [3]. Hydrogen seems to be a green, renewable energy carrier that can help solve the problems of non-sustainable energy use (fossil fuels). However, the efficient application of hydrogen requires careful consideration of the relevant safety concern. In fact, its physico-chemical properties make hydrogen a highly explosive gas [3,4]. Moreover, as hydrogen is colorless, odorless and tasteless, the ability to detect a hydrogen leak by means of selective sensors is highly desired.

Chemiresistive gas sensors based on semiconductor metal oxides have been drawing more and more attention because of their advantages such as low cost, lightweight, fast response/recovery times and high compatibility with microelectronic processing. Graphene and its derivatives, as well as some organic semiconductor-based materials constitute also an interesting family of chemo-resistive gas sensor due to their large surface area, good electrical, thermal and mechanical properties [5,6].

Cost effective metal oxide-based gas sensors such as  $\text{SnO}_2$ ,  $\text{WO}_3$ ,  $\text{ZnO}$ ,  $\text{NiO}$  or  $\text{CuO}$  operate mostly at temperatures below  $400^\circ\text{C}$  [7–10]. There are only few reports in literature focusing on their gas sensing above  $400^\circ\text{C}$ .  $\text{TiO}_2$  is one of them to be capable of operating above  $500^\circ\text{C}$ . The additional benefits of  $\text{TiO}_2$  are non-toxicity, easy fabrication, and the good chemical stability [11]. However,  $\text{TiO}_2$  is a high resistive n-type semiconductor with relatively poor conductivity for sensing oxidative gases such as  $\text{NO}_2$ . This disadvantage was previously reported to be overcome through addition of low valence dopant atoms which alter the electronic structure [12–15]. Another strategy is to use catalytically doped perovskite-based titanium compounds such as  $\text{BaTiO}_3$ . In this work, we report the synthesis of Co-doped  $\text{TiO}_2$ , Ni doped  $\text{TiO}_2$  and Rh-doped  $\text{BaTiO}_3$  by co-precipitation method and demonstrate gas sensing ability toward  $\text{NO}_2$ ,  $\text{NO}$  and  $\text{H}_2$  above  $500^\circ\text{C}$ . Our results yield that Co-doping of  $\text{TiO}_2$  promotes p-type behavior exhibiting good sensing properties to  $\text{NO}_2$  while Ni-doping displays the maintenance of n-type behavior and better  $\text{H}_2$ -sensing properties at  $600^\circ\text{C}$ . More interestingly, Rh-doped  $\text{BaTiO}_3$  shows excellent  $\text{NO}$  sensing properties even at  $900^\circ\text{C}$ .

## 2. Materials and Methods

### 2.1. Preparation of the Different Sensing Materials

Ni-doped  $\text{TiO}_2$  nanoparticles were prepared using the co-precipitation synthesis route followed by calcination. The starting precursor solutions were first prepared by dissolving nickel acetate in acetic acid while pure ethanol was used separately to dissolve titanium iso-propoxide (TTIP). The adjustment between the previously prepared nickel and titanium solution has been performed so that the final obtained mix would contain 0.0, 0.5, 1.0 and 2.0 mol.% of nickel dopant in  $\text{TiO}_2$  and were labeled as TN0, TN05, TN1 and TN2, respectively. The solutions were then mixed and stirred for 5 min. Oxalic acid was used as the precipitating agent. It was dissolved in absolute ethanol solution and poured progressively into the previously mixed solutions. In order to achieve a total precipitation, the resulting mixtures were stirred for 1 h at room temperature, followed by the filtration and drying of the obtained precipitate at  $80^\circ\text{C}$ . A white powder was obtained for the undoped precursor and a yellowish colored powder for the Ni-doped precursor samples. The prepared precursor powders were then calcined in a muffle furnace under static air for 3 h at  $700^\circ\text{C}$  to obtain the nano-particulate powders.

Co-doped  $\text{TiO}_2$  nanoparticles were synthesized by employing the same processing route. The cobalt acetate and titanium iso-propoxide solutions were adjusted to obtain 0.5 and 1 mol.% of cobalt in  $\text{TiO}_2$  and were labeled as 0.5Co-doped  $\text{TiO}_2$  and 1Co-doped  $\text{TiO}_2$ , respectively. The so-obtained precipitate was filtered and dried in oven at  $80^\circ\text{C}$  yielding a pink colored powder for the Co-doped samples.

The synthesis of Rh-doped  $\text{BaTiO}_3$  (designated as BTR1-OX-900) was also prepared by coprecipitation by following the same procedure. The amount of the aqueous Rh-nitrate solution, barium acetate and titanium iso-propoxide were adjusted to yield perovskites with the following composition:  $\text{BaTi}_{0.98}\text{Rh}_{0.02}\text{O}_3$ . The as-prepared precursor powder was calcined in a ceramic combustion boat holder at  $900^\circ\text{C}$  in a muffle furnace ( $5^\circ\text{C min}^{-1}$ ) for one hour under static air. In order to activate this material, it was treated under 2% of hydrogen at  $900^\circ\text{C}$  for two hours.

### 2.2. Materials Characterization

The XRD diffractograms of all the samples were obtained at room temperature with a D5000 Siemens Kristalloflex  $\theta$ – $2\theta$  powder diffractometer which has a Bragg-Brentano geometry and equipped with Cu-K $\alpha$  radiation ( $\lambda = 1.54178 \text{ \AA}$ ) and a standard scintillation counter detector.

Bruker Senterra Raman spectrometer (from Bruker Optik GmbH, Ettlingen, Germany) was used to record all the Raman spectra at room temperature under 532 nm and 0.2 mW power laser excitation, which was focused on samples through a 50X objective (Olympus MPlan N 50X/0.75).

The particles' morphology was determined by Scanning Electron Microscopic (SEM) analysis and was carried out in a Zeiss Ultra 55 microscope.

### 2.3. Sensor Preparation

The as prepared materials (Co-doped  $\text{TiO}_2$ , Ni-doped  $\text{TiO}_2$  and Rh-doped  $\text{BaTiO}_3$ ) powders were deposited as thick films ( $\sim 20 \mu\text{m}$ ) using a simple drop-coating method on alumina substrates that were previously fitted with interdigitated electrodes. The sensor response for n-type semiconductors is defined by  $(R_{\text{gas}}/R_{\text{air}} - 1) \times 100$  and  $(R_{\text{air}}/R_{\text{gas}} - 1) \times 100$  for oxidizing and reducing gases, respectively, while for p-type semiconductor,  $(R_{\text{gas}}/R_{\text{air}} - 1) \times 100$  and  $(R_{\text{air}}/R_{\text{gas}} - 1) \times 100$  for reducing and oxidizing gases respectively. R is the electrical resistance of the sensor material in air ( $R_{\text{air}}$ ) or in gas ( $R_{\text{gas}}$ )

### 3. Results and Discussion

The phase identification derived from powder XRD analysis is presented on Figure 1. As can be observed in Figure 1a for Ni-doped  $\text{TiO}_2$ , the results indicate that anatase is present in those from undoped to 1% Ni-doped  $\text{TiO}_2$ , while rutile is the only phase present in the 2% Ni-doped  $\text{TiO}_2$  powders. The amount of anatase (JCPDS 21-1272) decreases as the amount of nickel increases while the amount of rutile (JCPDS 21-1276) follows the opposite trend. A trace amount of ilmenite,  $\text{NiTiO}_3$  is observed at  $32.5^\circ$  in the TN1 and TN2 samples (JCPDS 33-0960). These results indicate that Ni promotes the transition of anatase to rutile. As far as Co-doped  $\text{TiO}_2$  is concerned, the results depicted on Figure 1b reveal that, the undoped and the 0.5Co-doped  $\text{TiO}_2$  samples showed pure  $\text{TiO}_2$  consisted of its two polymorphs; anatase (majority) and rutile phases (minority). No other phase containing Co was observed. The 1Co-doped  $\text{TiO}_2$  sample showed only single phase  $\text{TiO}_2$  but this time the rutile polymorph was the major phase as anatase phase was in trace amount. The X-ray results indicate that the cobalt dopant promotes also the anatase-to-rutile phase conversion of  $\text{TiO}_2$  but not progressively as nickel. The results of XRD analysis performed on the Rh-doped  $\text{BaTiO}_3$  (before and after the activation) are presented in Figure 1c. As shown, the major phase is  $\text{BaTiO}_3$  (according to JCPDS 075-0462) and a trace amount of  $\text{BaCO}_3$  phase is observed. No evidence of an Rh phase was encountered indicating the substitution of Ti by Rh.

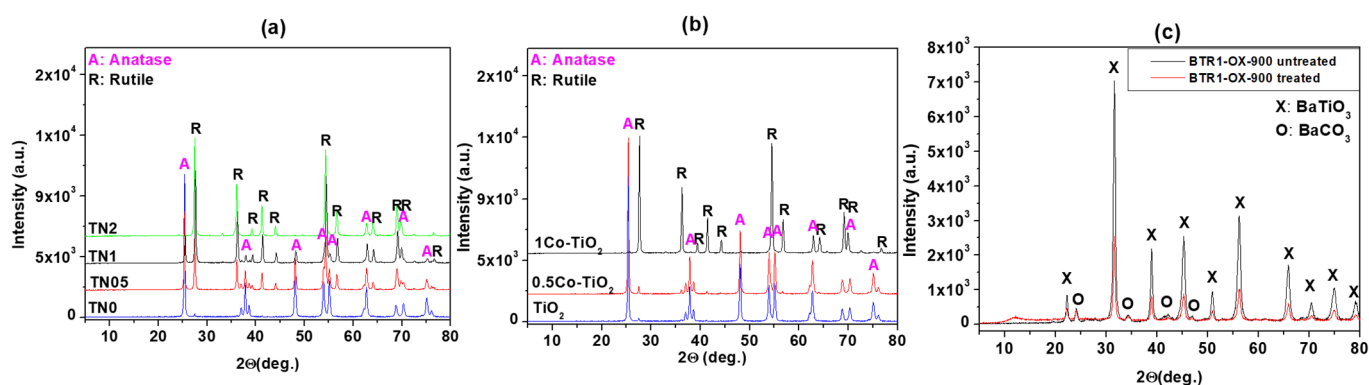


**Figure 1.** (a) Powder XRD patterns of Ni-doped  $\text{TiO}_2$ , (b) Co-doped  $\text{TiO}_2$  and (c) Rh-doped  $\text{BaTiO}_3$ .

Figure 2 shows the morphology of the synthesized powders investigated by SEM. Concerning Ni-doped  $\text{TiO}_2$  (Figure 2a), as far as the undoped powder sample is concerned, the microstructural investigation reveals spherical nanoparticles with sizes around 70 nm, which tend to agglomerate. While the TN05 sample shows more agglomerated spherical particles, the TN1 and TN2 samples show less agglomeration with the appearance of small pores and particle size reduction for the TN2 samples. Figure 2b shows the morphology of the Co-doped  $\text{TiO}_2$  synthesized powders. The SEM investigation revealed the formation of spherical nanoparticles with sizes around 70 nm. As the sample 0.5Co-doped  $\text{TiO}_2$  shows more agglomerated spherical particles, the sample 1Co-doped  $\text{TiO}_2$  presented larger and

well-faceted rhombohedral crystallites with less agglomeration. As SEM pictures display in Figure 2b the Rh-doped BaTiO<sub>3</sub> has the well-defined and homogeneously distributed spherical nanoparticles (~50 nm).

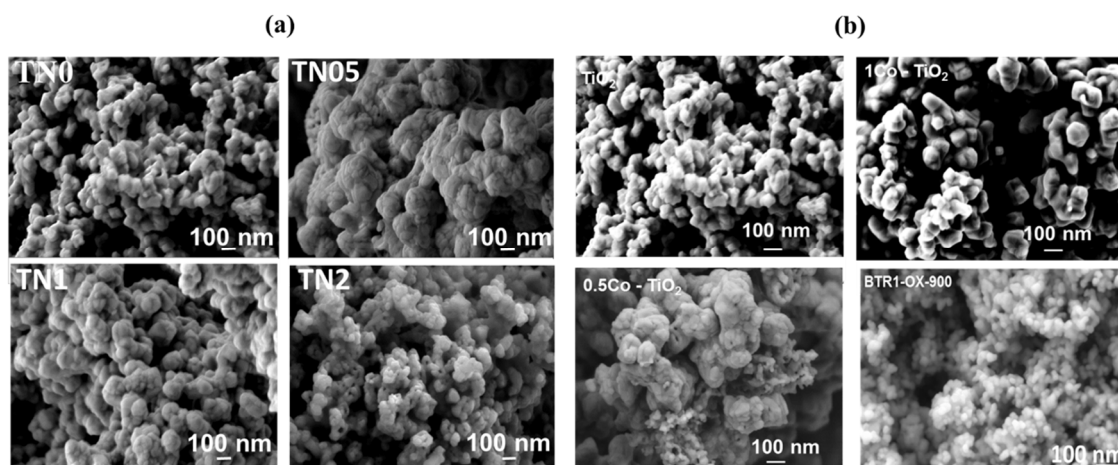


**Figure 2.** SEM images of (a) undoped and Ni-doped TiO<sub>2</sub> powders and (b) Co-doped TiO<sub>2</sub> and Rh-doped BaTiO<sub>3</sub>.

The Raman spectra of the samples were obtained between the wavenumbers of 175–800 cm<sup>−1</sup> and the results are presented in Figure 3. The results of Ni-doped TiO<sub>2</sub> Raman analysis (Figure 3a) show that the main signals came from TiO<sub>2</sub>. The samples TN0 and TN05 show very strong Raman signals, with peaks at 196(E<sub>g</sub>), 396(B<sub>1g</sub>), 517(A<sub>1g</sub>) and 638(B<sub>1g</sub>) cm<sup>−1</sup> from the typical anatase TiO<sub>2</sub> phase [16]. A weak peak at 447 cm<sup>−1</sup> (E<sub>g</sub>) attributed to rutile is observed in TN05. Samples TN1 and TN2, which contain larger amounts of Ni, present the Raman signals corresponding to both the anatase and rutile (447(E<sub>g</sub>), 612(A<sub>1g</sub>) cm<sup>−1</sup>) phase [17]. In addition to the anatase and rutile phases, another set of Raman vibrations emerges in the TN1 and TN2 samples. The peaks at 244, 345 and 706 cm<sup>−1</sup> are assigned to a trace amount of ilmenite, NiTiO<sub>3</sub>. In the Figure 3b showing the results of Co-doped TiO<sub>2</sub>, the Raman lines observed at 197, 390, 511, 637 cm<sup>−1</sup> can be assigned to E<sub>g</sub>, B<sub>1g</sub>, A<sub>1g</sub>, or B<sub>1g</sub> and E<sub>g</sub> modes of anatase phase respectively. The spectra show that the peak intensities decrease drastically after doping, due certainly to the decrease of the amount of anatase and the formation of rutile as indicated by XRD. Moreover, the Raman spectra of 1Co-doped TiO<sub>2</sub> yielded a smaller shift towards lower wavelengths while new peaks (436 cm<sup>−1</sup>) appeared indicating the presence of rutile polymorph, as mentioned in literature [17]. Raman spectra of Rh-doped BaTiO<sub>3</sub> are displayed in Figure 3c. It shows the peaks at 270, 308, 525 and 725 cm<sup>−1</sup> which are assigned respectively to the A<sub>1</sub>(TO<sub>2</sub>), E(TO<sub>2</sub>), A<sub>1</sub>(TO<sub>3</sub>), and A<sub>1</sub>(LO<sub>3</sub>) of barium titanate modes of the room temperature P4mm phase.

Based on our previous results on undoped, Al and Cr-doped TiO<sub>2</sub>, 600 °C was chosen as the optimum sensing temperature for Ni and Co doped TiO<sub>2</sub> in this work [12,13].



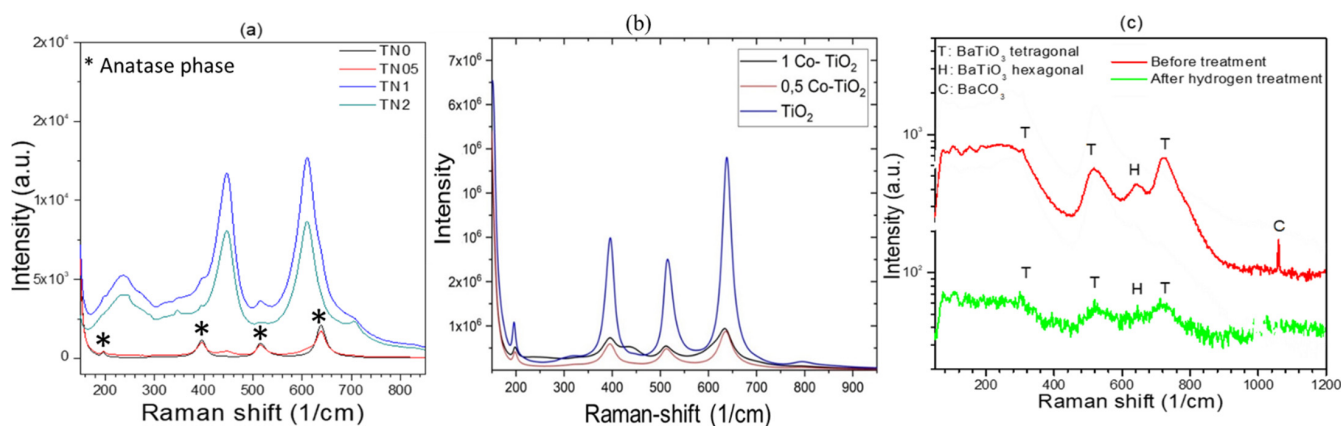


**Figure 3.** (a) Raman spectra of undoped and Ni-doped TiO<sub>2</sub>, (b) Co-doped TiO<sub>2</sub> and (c) Rh-doped BaTiO<sub>3</sub>.

The responses of the undoped TiO<sub>2</sub> and all Ni-doped TiO<sub>2</sub> towards 10,000 ppm H<sub>2</sub> in dry synthetic air at 600 °C are shown in Figure 4a. The sensor responses are 42, 72, 70 and 62% for TN0, TN05, TN1 and TN2, respectively. It can be observed that the sensor response increases greatly as Ni-content increases up to 0.5 mol.% and then decreases slowly with further increase in the Ni-content to 2.0 mol.%. This implies that the sensor reaches its maximum response of 72% with 0.5 mol.% of Ni dopant. It can be assumed that this enhancement of gas sensor response may be due to the formation of a n-n junction between the anatase ( $E_g = 3.2$  eV) and rutile ( $E_g = 3.0$  eV) phases. As revealed by XRD results, the TN05 sample contains almost the same amount of anatase and rutile phases (which is not the case with the other samples in this work), and thus, the highest amount of n-n junctions are expected to be present in this sample. This kind of junction effect has also been reported for other n-n junction systems such as ZnO-SnO<sub>2</sub> [18] and SnO<sub>2</sub>-WO<sub>3</sub> [19]. The achievement of a great selectivity towards the target gas is a key parameter and a very important characteristic. Therefore, the responses of the TN05 gas sensor towards a variety of interference gases including NO<sub>2</sub>, CO, and NO at 600 °C in dry synthetic air were explored to evaluate its selectivity. As observed in Figure 4b, the response of this sensor towards 600 ppm of H<sub>2</sub> (35%) is at least a factor of two higher than that towards 300 ppm of CO (12%), 300 ppm of NO<sub>2</sub> (11%) and 300 ppm of NO (7%). The sensor's H<sub>2</sub>-response was a factor of two greater compared to that for 300 ppm of all the tested interfering gases, yielding the highest value and indicating a relatively high selectivity potential of the sensor towards H<sub>2</sub>.

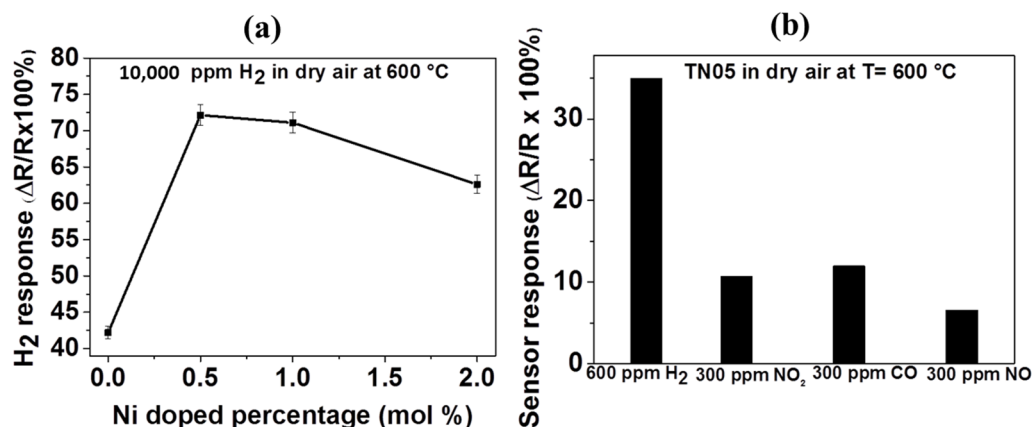


**Figure 4.** (a) Response of gas sensors based on undoped TiO<sub>2</sub> and Ni-doped TiO<sub>2</sub> to 10,000 ppm of hydrogen gas at the optimum operating temperature of 600 °C. (b) Response of gas sensor based on 0.5% Ni-doped TiO<sub>2</sub> to various gases including 600 ppm of H<sub>2</sub>, 300 ppm of NO<sub>2</sub>, NO and CO all in dry air at 600 °C.

As Figure 5a shows, the sensors yield higher response towards  $H_2$  than  $NO_2$ . The  $H_2$  sensor responses are 42, 23 and 33% for undoped, 0.5Co-doped  $TiO_2$  and 1Co-doped  $TiO_2$ , respectively. The undoped sample shows the highest response toward  $H_2$ . The presence of Co-dopant seems to decrease the  $H_2$ -sensing performance of  $TiO_2$  even though doping creates more oxygen vacancies in  $TiO_2$ . This behavior can be attributed to the increase of rutile polymorph content on doping with cobalt, as previously reported, rutile is the less active (in term of functional properties) polymorph of  $TiO_2$  [20]. On the other hand, the 1Co-doped  $TiO_2$  which contains predominantly rutile polymorph showed a higher response toward  $H_2$  than 0.5Co-doped  $TiO_2$ . This discrepancy can be explained by alteration of the conductivity from n-type to p-type. In fact, the dynamic response of the sensors toward  $H_2$  given in Figure 5b reveals that undoped and 0.5Co-doped  $TiO_2$  exhibit n-type semi-conductivity (i.e., their electrical resistance decreases upon interaction with hydrogen) while the 1Co-doped  $TiO_2$  yields p-type conductivity (its electrical resistance increases when reducing gas is introduced). The sensor responses measured toward the oxidizing gas  $NO_2$  were 5, 3 and 8% for undoped, 0.5Co-doped  $TiO_2$  and 1Co-doped  $TiO_2$  respectively. In the case of  $NO_2$  sensing, the 1Co-doped  $TiO_2$  showed the highest response. This may be mainly due to the electronic alteration of  $TiO_2$  from n to p-type semiconductor. Previous literature points out that this alteration can be utilized for the detection of oxidizing gas. Our current results confirm that the dominant factor for the gas sensing property of the Co-doped  $TiO_2$  depend on the existing polymorphs as well as the nature of target gas (oxidizing or reducing). In the case of reducing gases, the type of polymorphs has more influence on the gas sensitivity than the type of electronic structure, while an opposite trend can be observed for oxidizing gases.

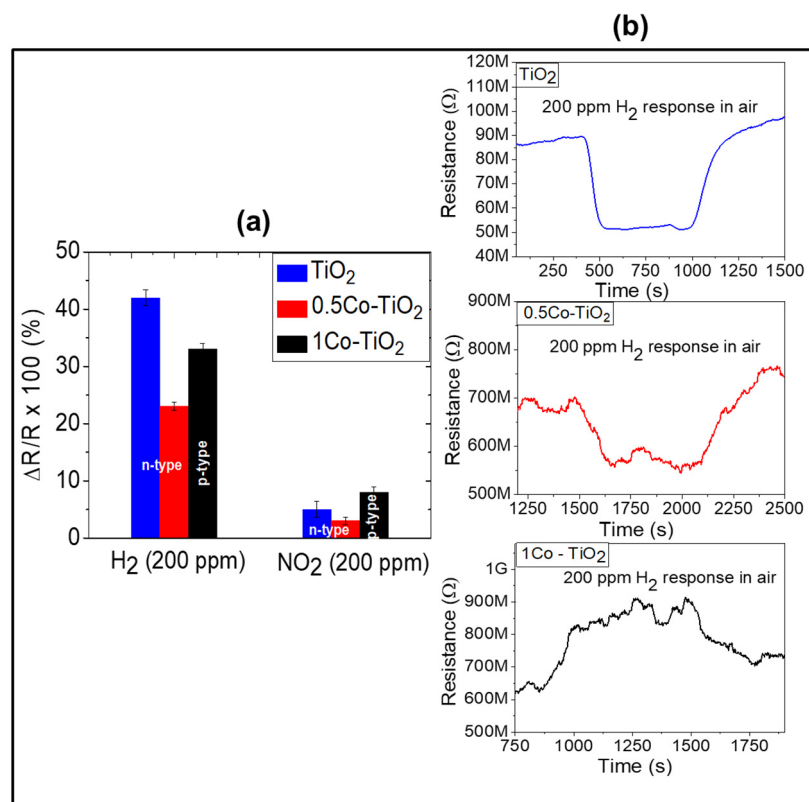


**Figure 5.** (a) Sensor response of undoped and Co-doped  $TiO_2$  towards  $NO_2$  and  $H_2$  at 600 °C and (b) their dynamic responses towards  $H_2$ .

Figure 6a shows the sensor responses of the hydrogen treated Rh-doped  $BaTiO_3$  towards 200 ppm of nitrogen oxide (NO) at a different operating temperature under dry and humid (10% of RH) synthetic air and the dynamic response at 700 and 900 °C, respectively. The sensor responses are 14, 2, 6, 7% in dry air, 6, 12, 16 and 18% in humid

air at 600, 700, 800, and 900 °C, respectively. In dry air, the sensor response decreases from 14 to 7% in general with the increasing temperature, while in humid air, the sensor response increases from 6 to 18% as the temperature increases. The maximum sensor response is therefore obtained at 900 °C under humidity. This enhancement of sensing properties in the presence of humidity can be explained by the affinity between adsorbed hydroxyl group (generated after thermal decomposition of water) and the NO. In fact, at high temperatures, H<sub>2</sub>O in water vapor decomposes, and hydroxyl is adsorbed on the sensing layer. As the temperature increases, more decomposition will occur, and more hydroxyl groups will be adsorbed on the surface, enhancing the NO sensor response. To the best of our knowledge, this is the first time that NO detection is reported at such a high temperature in the humid. Therefore, we have investigated intensely further gas sensing characteristics of this material under these extreme conditions (e.g., at 900 °C under humid air). Two other main products for fuel combustion are NO<sub>2</sub> and CO. Their presence in the exhaust gas stream at a high temperature can cause important hinderance for the NO gas sensing application. Our sensor's selectivity toward NO against CO and NO<sub>2</sub> at 900 °C under humid air was investigated. Figure 6b shows the different responses of the sensor to 200 ppm of NO, NO<sub>2</sub> and CO. The results indicate that at 900 °C, the response to 200 ppm of NO (18%) is higher than that of 200 ppm of NO<sub>2</sub> (8.7%) and 200 ppm of CO (8.4%). This implies that this sensor is at least twice as much sensitive to NO than NO<sub>2</sub> and CO. This good selectivity is ascribed to the catalytic effect of Rhodium-NPs on the oxidation of NO, which will promote and enhance the adsorption and the oxidation of NO preferentially. It is reported in the literature that Rhodium which is currently and often used in TWC, is a suitable catalyst for NO oxidation [21].

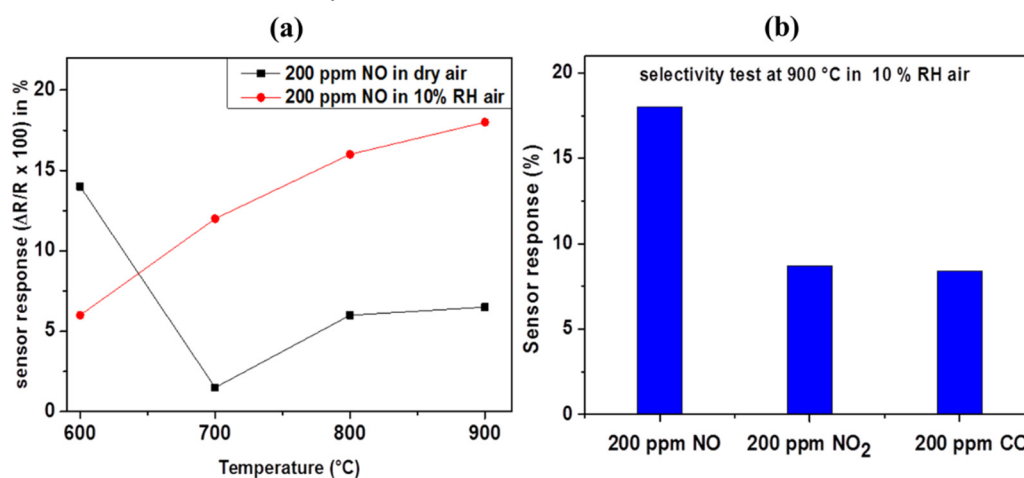


**Figure 6.** (a) Response of gas sensor based on activated Rh-doped BaTiO<sub>3</sub> to 200 ppm of NO in dry and humid air at different operating temperatures and (b) its selectivity investigation.

#### 4. Conclusions

This paper reports the successful synthesis of Ni-doped TiO<sub>2</sub>, Co-doped TiO<sub>2</sub> and Rh-doped BaTiO<sub>3</sub> nanoparticles by a facile co-precipitation route through the use of oxalic acid. Their NO<sub>2</sub>, NO and hydrogen sensing properties at high temperatures ( $\leq 600$  °C) were investigated. According to structural characterization the substitution of Ti<sup>4+</sup> by dopant (Ni<sup>2+</sup>, Co<sup>3+</sup> and Rh<sup>3+</sup>) was effective and creates more oxygen vacancies which promotes the anatase-to-rutile transformation in the case of Ni and Co doped TiO<sub>2</sub>. Enhanced sensing properties with respect to H<sub>2</sub> were observed for 0.5% Ni-doped TiO<sub>2</sub> in comparison to undoped and 1 and 2% Ni-doped TiO<sub>2</sub>. The sample 1Co-doped TiO<sub>2</sub> which reveals p-type conductive behavior yields an enhanced NO<sub>2</sub> response at 600 °C under air as carrier gas. With Rh-doped BaTiO<sub>3</sub>, it was possible to detect NO at 900 °C under humid air with a good response (18% for 200 NO ppm) and good selectivity (twice as much sensitive to NO than CO and NO<sub>2</sub>). Titanium based materials appear as a promising high temperature gas sensor in harsh environment.

**Author Contributions:** R.L.F.: conceptualization, data curation, formal analysis concerning Raman spectroscopy and SEM analysis, methodology and investigation concerning sensor testing, writing—original draft preparation; B.S.: supervision, project administration, funding acquisition, validation, visualization, writing—review and editing. All authors have read and agreed to the published version of the manuscript.

**Funding:** This research was funded by DAAD-DLR postdoc fellowship program, grant number 284.

**Institutional Review Board Statement:** Not applicable.

**Informed Consent Statement:** Not applicable.

**Data Availability Statement:** Data is contained within the article.

**Acknowledgments:** The authors thank Shujie You of the Luleå University of Technology in Sweden for the Raman spectroscopy measurements.

**Conflicts of Interest:** The authors declare no conflict of interest.

## References

1. Liu, Y.; Parisi, J.; Sun, X.; Lei, Y. Solid-state gas sensors for high temperature applications—A review. *J. Mater. Chem. A* **2014**, *2*, 9919–9943. [\[CrossRef\]](#)
2. Resitoglu, I.A. NOx Pollutants from Diesel Vehicles and Trends in the Control Technologies. *IntechOpen* **2018**, *3*, 1–16. [\[CrossRef\]](#)
3. Gu, H.; Wang, Z.; Hu, Y. Hydrogen gas sensors based on semiconductor oxide nanostructures. *Sensors* **2012**, *12*, 5517–5550. [\[CrossRef\]](#)
4. Hermawan, A.; Asakura, Y.; Kobayashi, M.; Kakihana, M.; Yin, S. High temperature hydrogen gas sensing property of GaN prepared from  $\alpha$ -GaOOH. *Sens. Actuators B Chem.* **2018**, *276*, 388–396. [\[CrossRef\]](#)
5. Singh, E.; Meyyappan, M.; Nalwa, H.S. Flexible Graphene-Based Wearable Gas and Chemical Sensors. *ACS Appl. Mater. Interfaces* **2017**, *9*, 34544–34586. [\[CrossRef\]](#)
6. Ali, S.; Gupta, A.; Shafiei, M.; Langford, S.J. Recent Advances in Perylene Diimide-Based Active Materials in Electrical Mode Gas Sensing. *Chemosensors* **2021**, *9*, 30. [\[CrossRef\]](#)
7. Dey, A. Semiconductor metal oxide gas sensors: A review. *Mater. Sci. Eng. B* **2018**, *229*, 206–217. [\[CrossRef\]](#)
8. Lontio Fomekong, R.; Tedjieukeng Kamta, H.M.; Ngolui Lambi, J.; Lahem, D.; Eloy, P.; Debliquy, M.; Delcorte, A. A sub-ppm level formaldehyde gas sensor based on Zn-doped NiO prepared by a co-precipitation route. *J. Alloys Compd.* **2018**, *731*, 1188–1196. [\[CrossRef\]](#)
9. Han, Y.; Liu, Y.; Su, C.; Chen, X.; Zeng, M.; Hu, N.; Su, Y.; Zhou, Z.; Wei, H.; Yang, Z. Sonochemical synthesis of hierarchical WO<sub>3</sub> flower-like spheres for highly efficient triethylamine detection. *Sens. Actuators B Chem.* **2020**, *306*, 127536. [\[CrossRef\]](#)
10. Cho, H.-J.; Choi, S.-J.; Kim, N.-H.; Kim, I.-D. Porosity controlled 3D SnO<sub>2</sub> spheres via electrostatic spray: Selective acetone sensors. *Sens. Actuators B Chem.* **2020**, *304*, 127350. [\[CrossRef\]](#)
11. Chen, X.; Mao, S. Titanium Dioxide Nanomaterials: Synthesis, Properties, Modifications, and Applications. *Chem. Rev.* **2007**, *107*, 2891–2959. [\[CrossRef\]](#) [\[PubMed\]](#)
12. Lontio Fomekong, R.; Saruhan, B. Synthesis of Co<sup>3+</sup> doped TiO<sub>2</sub> by co-precipitation route and its gas sensing properties. *Front. Mater.* **2019**, *6*, 252. [\[CrossRef\]](#)
13. Zhu, L.; Zhang, D.; Wang, Y.; Feng, C.; Zhou, J.; Liu, C.; Ruan, S. Xylene gas sensor based on Ni doped TiO<sub>2</sub> bowl-like submicron particles with enhanced sensing performance. *RSC Adv.* **2015**, *5*, 28105–28110. [\[CrossRef\]](#)
14. Gönüllü, Y.; Haidry, A.A.; Saruhan, B. Nanotubular Cr-doped TiO<sub>2</sub> for use as high-temperature NO<sub>2</sub> gas sensor. *Sens. Actuators B Chem.* **2015**, *217*, 78–87. [\[CrossRef\]](#)
15. Bayata, F.; Saruhan-Brings, B.; Ürgen, M. Hydrogen gas sensing properties of nanoporous Al-doped titania. *Sens. Actuators B Chem.* **2014**, *204*, 109–118. [\[CrossRef\]](#)
16. Chanda, A.; Rout, K.; Vasundhara, M.; Joshi, S.R.; Singh, J. Structural and magnetic study of undoped and cobalt doped TiO<sub>2</sub> nanoparticles. *RSC Adv.* **2018**, *8*, 912–916. [\[CrossRef\]](#)
17. Mazza, T.; Barborini, E.; Piseri, P.; Milani, P.; Cattaneo, D.; Li Bassi, A.; Bottani, C.E.; Ducati, C. Raman spectroscopy characterization of TiO<sub>2</sub> rutile nanocrystals. *Phys. Rev. B Condens. Matter.* **2007**, *75*, 045416. [\[CrossRef\]](#)
18. Chen, W.; Li, Q.; Xu, L.; Zeng, W. Gas sensing properties of ZnO-SnO<sub>2</sub> nanostructures. *J. Nanosci. Nanotechnol.* **2015**, *15*, 1245–1252. [\[CrossRef\]](#) [\[PubMed\]](#)
19. Van Toan, N.; Manh Hung, C.; Van Duy, N.; Duc Hoa, N.; Thanh Le, D.T.; Van Hieu, N. Bilayer SnO<sub>2</sub>–WO<sub>3</sub> nanofilms for enhanced NH<sub>3</sub> gas sensing performance. *Mater. Sci. Eng. B* **2017**, *224*, 163–170. [\[CrossRef\]](#)
20. Luttrell, T.; Halpegamage, S.; Tao, J.; Kramer, A.; Sutter, E.; Batzill, M. Why is anatase a better photocatalyst than rutile? Model studies on epitaxial TiO<sub>2</sub> films. *Sci. Rep.* **2014**, *4*, 4043. [\[CrossRef\]](#) [\[PubMed\]](#)
21. Weiss, B.M.; Artioli, N.; Iglesia, E. Catalytic NO Oxidation Pathways and Redox Cycles on Dispersed Oxides of Rhodium and Cobalt. *ChemCatChem* **2012**, *4*, 1397–1404. [\[CrossRef\]](#)